The Long-term Corrosion Behaviors of SLM 316L Stainless Steel Immersed in Artificial Saliva

Yanmei LI, Chiate LIU *, Yaohua LIANG, Xiaotong CHEN, Zhibiao YANG, Yingjun CHEN

School of Electronic and Electrical engineering, Zhaoqing University, Ying Bin Avenue, Zhaoqing 526061, Guangdong, China

The Selective Laser Melting (SLM) is an effective method to produce highly corrosion resistant Oral Alveolar Implants (OAI) by changing the scanning speed. Nevertheless, the long-term corrosion behavior of SLM 316L orthodontic bracket alloys in artificial saliva is overlooked in previous studies. In this study, 316L SS samples fabricated by SLM at different scanning speeds (800 mm/s, 1200 mm/s, and 1600 mm/s) were conducted a long-term (90 days) immersion test by being put into artificial saliva with three different pH values (pH 1.5, pH 4, and pH 6). The morphology, XRD and especially corrosion behavior of the samples fabricated by SLM and forging were investigated. The XRD results exhibit that high-speed scanning accelerates the cooling rate and inhibits the $\delta \rightarrow \gamma$ phase transformation proceeding. Corrosion results show that the corrosion attack induced by pre-existing pores will expand through the crevices and break down the surface structure around the pores, leading to corrosion damage area to expand to several times of the original pore area. Besides, the mean corrosion rate of the sample at a scanning speed of 800 mm/s shows better corrosion resistance in artificial saliva of pH 4 and pH 6. Compared with wrought 316L SS samples, the SLM 316L SS samples had an obvious difference in the performance of corrosion rate and corrosion behaviors.

Keywords: corrosion behaviors, SLM, scanning speed, artificial saliva.

1. INTRODUCTION

Implant materials have been developed to replace diseased or damaged parts in the human body in order to prolong life, to improve and restore tissue function, and to improve quality of life [1]. There are two requirements for implant materials, which are good biocompatibility and long-term stability. In contemporary orthodontic treatment, the implant materials are mainly including metal, plastic, and ceramic [2]. The widely used metal implant materials are stainless steel, cobalt-based alloy, Ti and Ti alloys, etc. [3, 4]. AISI 316L SS is a common implant material because of its reasonable cost, easy accessibility, excellent manufacturing properties, accepted biocompatibility, and good performance in corrosion resistance, making this material is extremely attractive in the application of implant materials [5].

In recent years, the technology of metal additive manufacturing has played important roles in biological and medical fields [6]. Selective Laser Melting (SLM) is one of the most common technologies in metal additive manufacturing. It adapts laser beam with high energy density as input resources, forms three-dimensional digital mode in Z axis through melting and solidifying metal powder in each layer, and then transforms real parts. Flexible manufacturing of complex parts can be achieved and it skips to be manufacturing technology with the most advanced and potential applications. Compared with conventional technologies, SLM technology can produce complex, high precision, and higher density parts directly, providing wider freedom for designing and applications [7].

While, although SLM implants have excellent structure and machinery performances, needless to say, unavoidable corrosion issues are hidden as well in various environments for this material. It is reported that the failures of metal implants are mainly caused by a fracture in 42 %, corrosion in 24 %, and vicious organization along with the implants in 14 % [8]. Hence, when applying SLM technology to biology implants, corrosion issues seem especially significant [9].

Among the researches that discussing corrosion behaviors of SLM samples in different environments, Wen et al. researched corrosion behaviors of SLM S136 SS samples and casting samples after immersion in 6 % FeCl₃ solution for 48 hours [10]. The results pointed out that SLM samples had better anti-corrosion performance, but with deeper corrosion pits compared with casting samples. Zhang et al. researched on the corrosion properties of SLM Ti-6Al-4V alloy after immersion in simulated seawater for $1 - 5$ weeks in the method of electrochemical impedance measurement [11]. The results showed the SLM Ti-6Al-4V alloy with fine grains structure could form dense TiO_2 films in the beginning, which allowed this alloy with better anti-corrosion performance, compared with wrought Ti-6Al-4V alloy, in the immersion period.

Based on the above researches, most of the experiments were conducted by adapting short time immersion tests. To observe the corrosion behaviors of SLM samples in the biological environment as real as possible, according to previous research [12], a long-term immersion test was used in this investigation. The corrosion properties of SLM 316L SS samples in artificial saliva with various pH values were studied and compared with wrought 316L SS

---

* Corresponding author. Tel.: +8613859126798.
E-mail address: *2019010037@zqu.edu.cn* (C. Liu)

samples through experimental tests and theoretical analysis methods. The findings are expected to contribute valuable information for developing SLM 316L materials for broader Oral Alveolar Implant application.

2. MATERIALS AND METHODS

2.1. Materials

The raw material used in this investigation was gas-atomized 316L SS spherical powder. The morphology and particle size distributions are shown in Fig. 1. The maximum particle diameter of powder is below 50 μm, and the mean particle diameter is 25.88 μm. In addition, wrought 316L SS after heat treatment is selected as reference material.
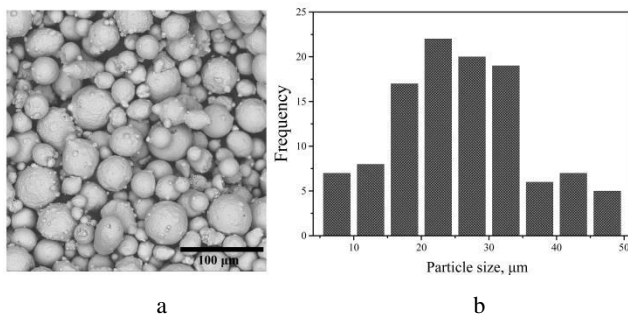

a   b

Fig. 1. a – SEM micrographs showing the morphology of the 316L powder; b – the particle size distribution

2.2. SLM machine and process parameters

An SLM machine (BLT-S200, BLT, China) equipped with a 200W Yb:YAG fiber laser was used to fabricate the SLM samples in this study. The thickness of the layer ranges from 20 to 60 μm. The stripe scanning strategy was applied, and the stripe was rotated by 67° counterclockwise for each layer. Scanning speed has an important influence on the performance of SLM samples. In this study, the values of other process parameters are fixed, three different values (800 mm/s, 1200 mm/s, and 1600 mm/s) are used for scanning speed.

2.3. Characterization

The qualitative analysis of SLM samples is performed by using X-ray diffractometry (XRD). The device uses Cu as a target, with 40 kV voltage values and 40 mA current values. The diffraction angle of 2θ varied from 40° to 95° at 10°/min scanning speed. The microstructures were observed by using optical microscopy (OM) and scanning electron microscopy (SEM) equipped with an EDS detector. Metallographic treatment of samples was cut at first, followed by a hot mounting, grinding, and polishing. A reagent consisting of HNO_3 and HCl in the ratio of 1:3 was used as an etching solution.

2.4. Immersion corrosion test

Immersion test samples in this study contain SLM 316L SS in three different scanning speeds and wrought 316L SS as reference material. Two groups of samples are prepared following ASTM G31-2012A. Before the immersing test, drying samples are weighed (accuracy of 0.1 mg) at first, then samples hung by nylon strings are fully immersed into glass containers filled with test solution independently, and covered by silica gels tightly, as shown in Fig. 2. After this, put them into a constant temperature drying oven at 37 ± 0.5 °C.

Fig. 2. Immersion specimens in aglass container covered with silicone plug

Test solution adapts artificial saliva at different pH values. The chemical compositions of artificial saliva include NaCl, KCl, $CaCl_2$, NaH_2PO_4, Urea, Na_2S, and distilled water. Normally the pH value of natural saliva is near neutral, but it would reduce to pH 2 depending on consumed foods or beverages [13]. In this study, three pH values of artificial saliva (pH 1.5, pH 4, and pH 6 adjusted by NaOH and HCl) were selected to investigate the corrosion behavior of SLM 316L SS in more severe environments. The ratio of solution volume and sample area is 0.20 ml/mm².

A long-term immersion time (90 days) was carried out in this study. During the duration, the test solutions in glass containers would be checked one time per two days, to ensure the normal solution level. After immersion, the samples were cleaned to remove corrosion products, and reweighed after totally drying. The corrosion rate is calculated based on the below formula after obtaining final weight losses (g).

$$\text{Corrosion rate (mm/y)} = \frac{8.76 \times 10^4 \times W}{D \times A \times T}, \qquad (1)$$

where W is weight losses of the samples, g; D is density, g/cm³; A is surface area, cm²; T is experiment time, h.

3. RESULTS AND DISCUSSION

3.1. Microstructural properties

Fig. 3 is the XRD diffraction patterns of 316L SS powder and SLM 316L SS samples in different scanning speeds. The experiment result of 316L SS powder samples is similar to the results from previous researches [14, 15], showing a fully γ phase structure. Compared with powder samples, the diffraction peaks of SLM samples appear different in two aspects. Firstly, the peak of SLM samples is a little wider than that of powder samples. It can be attributed to the rapid heating/cooling rate during SLM processes, certain residual stresses and dislocations storage in the material, and induced grain lattice distortion [16]. Secondly, different from powder samples with a fully γ phase, SLM samples also include some δ phases in the low angle position (the magnification part in Fig. 3). Based on the Fe-C equilibrium diagram, the δ phase is the structure locating in the high temperature zone. While, due to the cooling rate of the SLM process can reach 10⁵ K/s [17], the

time from melting state to solid state is too short for δ state to transform to γ phase [18, 19]. In addition, from Fig. 3, it can be observed as well that the δ phase peak's intensity of SLM 316L SS sample in 800 mm/s is lower than that in 1200 mm/s and 1600 mm/s.
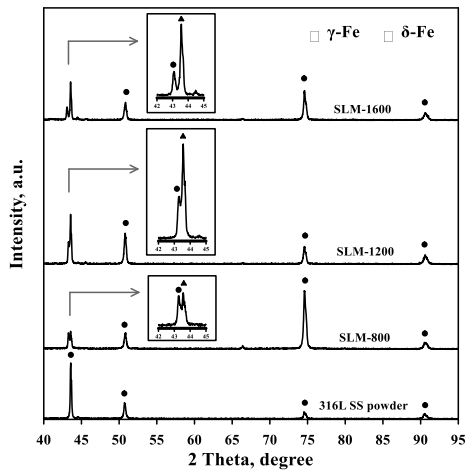

Fig. 3. XRD patterns of 316L SS powder and SLM 316L SS fabricated in scanning speed of 800, 1200, and 1600 mm/s

This is attributed to the fact that high-speed scanning accelerates the cooling rate and inhibits the δ → γ phase transformation proceeding.

Fig. 4 shows the SLM 316L SS sample surface morphology observed by OM (Fig. 4 a, b and c) and SEM (the enlarged part in the upper right corner of Fig. 4 b and d). It can be seen from the figure that the SLM 316L SS sample with a scanning speed of 800 mm/s has an obvious directional hatch space. When the scanning speed is increased to 1200 and 1600 mm/s, the hatch space reduces significantly or even disappears. Moreover, the sample of 1600 mm/s shows pores distribution with varying sizes, the largest being over 100 μm. After further observation, it can be found that these pores show non-spherical morphology while some of them still contain unmelted powders, as shown in Fig. 4 d.
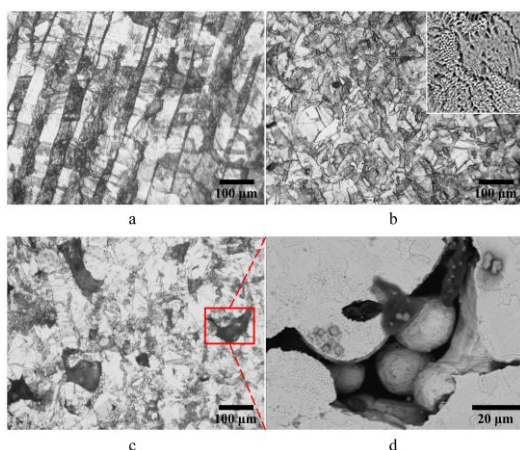

Fig. 4. Images of SLM 316L SS samples in different scanning speeds: a – 800; b – 1200 mm/s; c – 1600 mm/s; d – the enlarged micrographs of the marked pore on image c

Thus, it can be deduced that these pores are process-induces porosity, usually caused by laser power being too low or scanning speed being too fast, leading to the laser energy exerted on the powder bed being not dense enough, hence forming the so-called lack of fusion defects [20 – 22]. In addition, it can be observed from Fig. 4 that there are bright and dark areas distributed on the three SLM samples. The brighter areas are γ phase matrix and the darker areas are mainly cell clusters consisted of fine anisotropic equiaxed grains and isotropic columnar grains, as shown in Fig. 4 b. Such microstructures are mainly caused by rapid solidification and high thermal gradients during the SLM processes. More details about these microstructures have been discussed in the literature [23]. It is worth mentioning that these fine cellular structures show relatively even distribution on SLM 316L SS samples in scanning speeds of 800 and 1200 mm/s, while less even on the sample of 1600 mm/s. It is reported that austenitic grains with fine cellular structures and homogeneous constituent distribution resulted in better mechanical properties and corrosion resistance for SLM samples [24].

3.2. Corrosion behavior

3.2.1. Corrosion rate

Table 1 lists the designated numbers of SLM samples and wrought samples, as well as the corrosion rate results calculated from weight loss after the samples have been through immersion experiment. Fig. 5 is the trend graph of the mean corrosion rate obtained from Table 1. From overall data and trend, it can be concluded that the mean corrosion rate of SLM samples is higher than wrought samples in the same pH test solution. On the other hand, the mean corrosion rate of SLM samples increases as the pH value of the test solution decreases under the same scanning speed. The corrosion rate of the S1600-1 sample can be as high as 0.746 mm/y, exceeding all other samples. Except for high porosity and strong acid factors, it can also result in the uneven cell cluster distribution and the certain amount of δ phases contained in the sample. Some reported researches point out that when a certain amount of δ phase exists in austenitic stainless steel, it will lower the concentration of Cr and Mo of γ phase, causing the stability of passive film to degrade [25, 26].

Additionally, it is worth mentioning that the mean corrosion rate of samples in scanning speed of 800 and 1200 mm/s has an irregular correlation with the pH value. In pH 4 tested solution, the mean corrosion rate of sample in scanning speed of 1200 mm/s is slightly higher than that in scanning speed of 800 mm/s; however, in pH 1.5 and pH6 tested solution, the mean corrosion rate of sample in scanning speed of 1200 mm/s is instead lower than that in scanning speed of 800 mm/s. Thus, it can be deduced that it may be related to the uneven porosity distribution in the 1200 mm/s sample. Overall, for SLM samples, porosity increases as scanning speed increases while corrosion rate shows the same trends with the change in porosity.

3.2.2. Corrosive surface morphology

Fig. 6 shows the corrosion surface morphology of the SLM sample of a scanning speed of 1600 mm/s. The figure shows that, in the three pH-value environments, those irregular-shape pores formed at high scanning speed are the initialization positions for corrosion damage. The reason is that the oxide films on the side walls of these pre-existed

pores are less protective at the test solution, metal dissolution can take place here higher and hard to diffuse out of pores.

Table 1. The corrosion rate of SLM and wrought 316L samples in artificial saliva with variable pH values for 90 days

Samples	Scanning speed, mm/s	pH value of AS	Mean corrosion rate, mm/y
S1600-6	1600	6	0.199
S1600-4	1600	4	0.598
S1600-1	1600	1.5	0.671
S1200-6	1200	6	0.110
S1200-4	1200	4	0.211
S1200-1	1200	1.5	0.236
S800-6	800	6	0.134
S800-4	800	4	0.182
S800-1	800	1.5	0.322
W-6	–	6	0.009
W-4	–	4	0.066
W-1	–	1.5	0.149

Hence, the anolyte inside the pores becomes more aggressive, leading to the destruction of passivity [27].

Moreover, corrosion attack with larger scale continues to expand through the crevices and cause cracks around the pores and finally leading to the surface structure metal to gradually break down and peel off. This phenomenon can be observed clearly from the exposed metal sub-surface around the pores, as shown in Fig. 6. Because the sub-surface is only protected by a thin passive film, pits damage can be observed here. SLM samples present more or less this kind of corrosion damaged characteristics, especially obvious in acidic solution. However, for wrought samples, only near-surfaced metal flakes can be found to break away in localized areas, as shown in Fig. 7, completely different from the SLM samples. Still, these areas lack the protection of passivation film hence more easily damaged by corrosion, which can be seen from the different extent of pit corrosion experienced by the three sets of samples in Fig. 7 in different pH-value solutions.
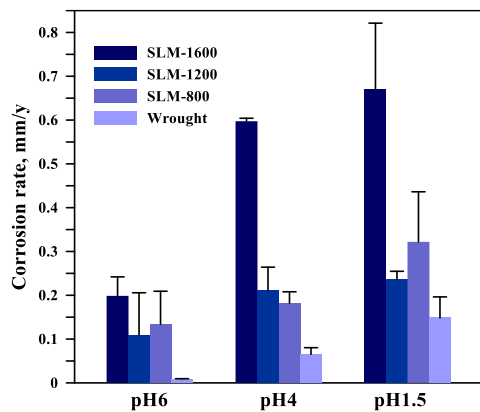

Fig. 5. The difference between the corrosion rate of the samples

Table 2 shows the EDS analysis results at the positions in Fig. 6. The results show that the concentration of Fe and Cr at these three positions (marked as 1, 4, 6) are lower by 4~5 wt.% as compared to other areas, while the concentration of O is higher by 5~7 wt.% as compared to other areas. This proves that after the surface oxides (iron oxides and chromium oxides mainly) in the pores have been

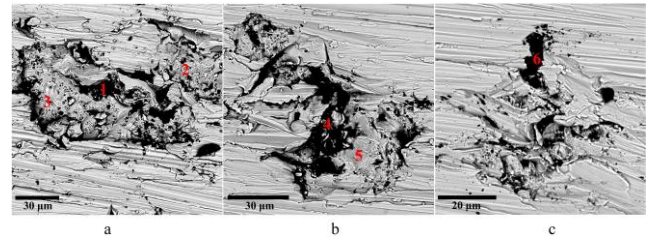dissolved, some Fe and Cr ions dissolving out from the samples.

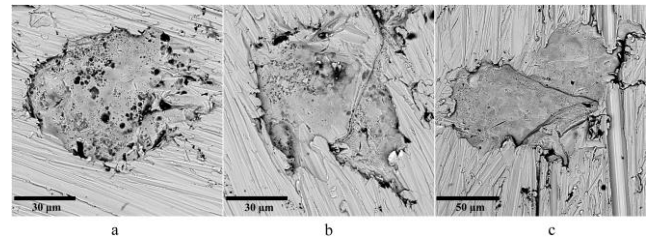**Fig. 6.** SEM micrographs showing the surface morphology of the samples: a – S1600-1; b – S1600-4; c – S1600-6

Fig. 7. SEM micrographs showing the surface morphology of the samples: a – W-1; b – W-4; c – W-6
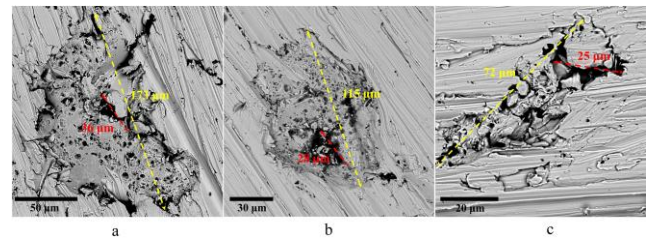

Fig. 8. SEM micrographs showing the surface morphology of the samples: a – S1600-1; b – S1200-4; c – S800-6
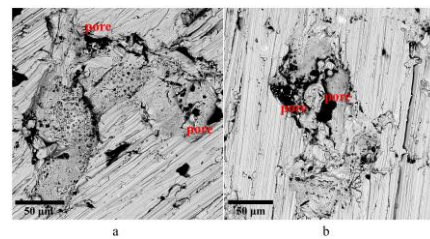

Fig. 9. SEM micrographs showing the surface morphology of the samples: a – S1600-1; b – S1600-6

Meanwhile, it is accompanied by dissolved oxygen adsorbed onto the surface. Moreover, locations marked as 2, 3, 5 in Fig. 6 are the positions of exposed sub-surface after corrosion damage. It can be seen that the concentration of oxygen at these three positions is reduced as compared to other areas, which shows that the passivation film of the sub-surface is rather thin and the re-passivation capability is rather weak, corrosion resistance being rather weak as well. It is worth mentioning that, relatively high Mn (0.99 wt.%) and S (0.64 wt.%) are detected at position 5, which means that MnS inclusions are precipitated at the sub-surface.

The effect of pH value on corrosion depends on the situation with or without pre-existing pores. For a situation without pores, the metal corrosion rate at the anode depends on the reaction at the cathode. When the pH value of the solution between 4 and 6, the corrosion rate is mainly governed by the depolarization at which oxygen reacts with

adsorbed atomic hydrogen on the surface; when the pH value of the solution is decreased to 1.5, the concentration of H⁺ increases, the corrosion rate not only depends on depolarization by oxygen, but also hydrogen evolution [28].

Table 2. EDS analysis results of marked positions in Fig. 6

Elements, wt.%	Locations					
	1	2	3	4	5	6
Fe	61.14	66.61	66.39	61.43	66.38	62.27
Cr	15.21	16.10	15.93	15.08	16.88	15.26
Ni	10.97	9.44	9.60	10.98	8.07	9.42
O	8.98	3.95	4.24	8.14	3.25	10.57
Mo	2.05	2.02	1.99	2.22	0.96	1.56
Si	0.77	0.95	0.83	1.01	0.82	0.21
Mn	0.73	0.76	0.83	0.80	0.99	0.63
S	0.15	0.17	0.19	0.34	0.64	0.08
Cl	–	–	–	–	2.01	–

The two reactions happen simultaneously at the cathode, speeding up the metal dissolution at the anode and leading to a relatively rigorous corrosion reaction. Such corrosion behaviors dominated by pH value are shown obviously on the wrought samples in this study. For the situation with pre-existing pores, i.e. SLM samples, except for acidic solution will accelerate the crevices corrosion and cause serious damage on the sub-surface as mentioned above, moreover, deeper pores or crevices also causes increasing acidic concentration and worsening the corrosion damage [29, 30].

Research points out, pores are the primary positions for corrosion in SLM material [31]. While, the corrosion reaction induced by pores not only damages the material's surface vertically, but also widens the scale of impact horizontally. Fig. 8 shows the situation of surface corrosive damage induced by single-pore corrosion, comparing the maximum length of the pore (red marked areas) and the maximum length of corroded area (yellow marked areas), its damage can extend to 4 – 5 times, even the pore is smaller than 30 μm. Schaller et al. pointed out, for SLM stainless steel, when the diameter of pore ≥ 50 μm, corrosion resistance decreased significantly [32]. This is slightly different from the results observed in this study. It is deduced that except for the difference in materials used, it can also be due to the long-term immersion experiment adopted in this study. Fig. 9 shows when multiple pores (red marked areas) come close to each other, after long-term immersion, some areas of corrosion will combine to form larger areas, causing the corrosive damage reaction to become more rigorous.

4. CONCLUSIONS

1. XRD analysis results show SLM 316L SS samples commonly exhibit fine-grained microstructures and certain untransformed δ phases. This is due to the SLM fast heating/cooling process that inhibits the grain growth and δ phase transformation proceeding.
2. Immersive corrosion experiment results show under the same pH values, the mean corrosion rate of SLM samples is higher than that of the wrought samples; while under the same with a scanning speed, the mean corrosion rate of SLM samples increases as the pH value of corrosion decreases.

3. The SLM sample in scanning speed of 1600 mm/s has the highest corrosion rate when immersed in pH1.5 artificial saliva, which is mainly due to the high porosity of this sample that provides favorable corrosion conditions in an acidic environment. Other reasons may include partially untransformed δ phases and uneven distribution of cell clusters.
4. Under long-term immersion test, the corrosion damage area induced by pores can expand to several times the original pore area. When multiple pores come close to each other, individual corroded areas will combine to form larger areas causing the corrosive damage to have a more severe impact.

REFERENCES

1. **Singh, R., Dahotre, N.B.** Corrosion Degradation and Prevention by Surface Modification of Biometallic Materials *Journal of Materials Science Materials in Medicine* 18 2007: pp. 725 – 751.
https://doi.org/10.1007/s10856-006-0016-y

2. **Zhao, Z., Li, J., Bai, P., Qu, H., Liang, M., Liao, H., Wu, L., Huo, P., Liu, H., Zhang, J.** Microstructure and Mechanical Properties of TiC-Reinforced 316L Stainless Steel Composites Fabricated Using Selective Laser Melting *Metals* 9 (2) 2019: pp. 267.
https://doi.org/10.3390/met9020267

3. **Kong, D., Ni, X., Dong, C., Lei, X., Zhang, L., Man, C., Yao, J., Cheng, X., Li, X.** Bio-functional and Anti-corrosive 3D Printing 316L Stainless Steel Fabricated by Selective Laser Melting *Materials and Design* 152 2018: pp. 88 – 101.
https://doi.org/10.1016/j.matdes.2018.04.058

4. **Ali, S., Abdul-Rani, AM., Baig, Z., Ahmed, SW., Hussain, G., Subramaniam, K., Hastuty, S., Tadamilla Rao, V.V.L.N.** Biocompatibility and Corrosion Resistance of Metallic Biomaterials *Corrosion Reviews* 38 2020: pp. 381 – 402.
https://doi.org/10.1515/corrrev-2020-0001

5. **Gotman, I.** Characteristics of Metals Used in Implants *Journal of Endourology* 11 (6) 1997: pp. 383 – 389.
https://doi.org/10.1089/end.1997.11.383

6. **Ventola, C.L.** Medical Applications for 3D Printing: Current and Projected Uses *P & T : A Peer-reviewed Journal for Formulary Management* 39 (10) 2014: pp. 704 – 711.

7. **Herzog, D., Seyda, V., Wycisk, E., Emmelmann, C.** Additive Manufacturing of Metals *Acta Materialia* 117 2016: pp. 371 – 392.
https://doi.org/10.1016/j.actamat.2016.07.019

8. **Sailer, I., Philipp, A., Zembic, A., Pjetursson, B.E., Hammerle, C.H.F., Zwahlen, M.** A Systematic Review of the Performance of Ceramic and Metal Implant Abutments Supporting Fixed Implant Reconstructions *Clinical Oral Implants Research* 20 2009: pp. 4 – 31.
https://doi.org/10.1111/j.1600-0501.2009.01787.x

9. **Eliaz, N.** Corrosion of Metallic Biomaterials: A Review *Materials* 12 2019: pp. 407 – 498.
https://doi.org/10.3390/ma12030407

10. **Wen, S.F., Ji, X.T., Zhou, Y., Han, C.J., Wei, Q.-S., Shi, Y.-S.** Corrosion Behavior of the S136 Mold Steel Fabricated by Selective Laser Melting *Chinese Journal of Mechanical Engineering* 31(06) 2018: pp. 68 – 78.
https://doi.org/10.1186/s10033-018-0312-8

11. **Zhang, Y., Li, J., Xu, H., Feng, L., Zhang, T.** Dynamic Evolution of Oxide Film on Selective Laser Melted Ti-6Al-4V Alloy *Journal of Alloys and Compounds* 849 2020: pp. 156622.
https://doi.org/10.1016/j.jallcom.2020.156622

12. **Chen, C.H., Ou, K.L., Wang, W.N.** Variation in Surface Morphology and Microstructure of 316L Biomedical Alloys Immersed in Artificial Saliva *Journal of Experimental & Clinical Medicine* 5 (1) 2013: pp. 30 – 36.
https://doi.org/10.1016/j.jecm.2013.01.008

13. **Koike, M., Fujii, H.** The Corrosion Resistance of Pure Titanium in Organic Acids *Biomaterials* 22 (21) 2001: pp. 2931 – 2936.
https://doi.org/10.1016/S0142-9612(01)00040-0

14. **Zhong, Y., Liu, L., Wikman, S., Cui, D., Shen, Z.** Intragranular Cellular Segregation Network Structure Strengthening 316L Stainless Steel Prepared by Selective Laser Melting *Journal of Nuclear Materials* 470 2016: pp. 170 – 178.
https://doi.org/10.1016/j.jnucmat.2015.12.034

15. **Choi, J.P., Shin, G.H., Brochu, M., Kim, Y.J., Yang, S.S., Kim, K.T., Yang, D.Y., Lee, C.W., Yu, J.H.** Densification Behavior of 316L Stainless Steel Parts Fabricated by Selective Laser Melting by Variation in Laser Energy Density *Materials Transactions* 57 (11) 2016: pp. 1952 – 1959.
https://doi.org/10.2320/matertrans.M2016284

16. **Wang, D., Song, C., Yang, Y., Bai, Y.** Investigation of Crystal Growth Mechanism during Selective Laser Melting and Mechanical Property Characterization of 316L Stainless Steel Parts *Materials and Design* 100 2016: pp. 291 – 299.
https://doi.org/10.1016/j.matdes.2016.03.111

17. **Prashanth, K.G., Debalina, B., Wang, Z., Gostin, P.F., Gebert, A., Calin, M., Kühn, U., Kamaraj, M., Scudino, S., Eckert, J.** Tribological and Corrosion Properties of Al-12Si Produced by Selective Laser Melting *Journal of Materials Research* 29 2014: pp. 2044 – 2054.
https://doi.org/10.1557/jmr.2014.133

18. **Sun, Z., Tan, X., Tor, S.B., Yeong, W.Y.** Selective Laser Melting of Stainless Steel 316L with Low Porosity and High Build Rates *Materials and Design* 104 2016: pp. 197 – 204.
https://doi.org/10.1016/j.matdes.2016.05.035

19. **Tucho, W.M., Lysne, V.H., Austbø, H., Sjolyst-Kverneland, A., Hansen, V.** Investigation of Effects of Process Parameters on Microstructure and Hardness of SLM Manufactured SS316L *Journal of Alloys and Compounds* 740 2018: pp. 910 – 925.
https://doi.org/10.1016/j.jallcom.2018.01.098

20. **Sames, W.J., List, F.A., Pannala, S., Dehoff, R.R., Babu, S.S.** The Metallurgy and Processing Science of Metal Additive Manufacturing *International Materials Reviews* 61 (5) 2016: pp. 315 – 360.

https://doi.org/10.1080/09506608.2015.1116649

21. **Teng, C., Pal, D., Gong, H., Zeng, K., Briggs, K., Patil, N., Stucker, B.** A Review of Defect Modeling in Laser Material Processing *Additive Manufacturing* 14 2017: pp. 137 – 147.
https://doi.org/10.1016/j.addma.2016.10.009

22. **Yusuf, S.M., Chen, Y., Boardman, R., Yang, S., Gao, N.** Investigation on Porosity and Microhardness of 316L Stainless Steel Fabricated by Selective Laser Melting *Metals* 7 (2) 2017: pp. 64.
https://doi.org/10.3390/met7020064

23. **Wang, G., Liu, Q., Rao, H., Liu, H., Qiu, C.** Influence of Porosity and Microstructure on Mechanical and Corrosion Properties of a Selectively Laser Melted Stainless Steel *Journal of Alloys and Compounds* 831 2020: pp. 154815.
https://doi.org/10.1016/j.jallcom.2020.154815

24. **Sing, S.L., An, J., Yeong, W.Y., Wiria, F.E.** Laser and Electron-beam Powder-bed Additive Manufacturing of Metallic Implants: A Review on Processes, Materials and Designs *Journal of Orthopaedic Research* 34 2016: pp. 369 – 385.
https://doi.org/10.1002/jor.23075

25. **Kim, S.Y., Kwon, H.S., Kim, H.S.** Effect of **D**elta **F**errite on Corrosion Resistance of Type 316L Stainless Steel in Acidic Chloride Solution by Micro-droplet Cell *Solid State Phenomena* 124 – 126 2007: pp. 1533 – 1536.
https://doi.org/10.4028/www.scientific.net/SSP.124-126.1533

26. **Bai, G., Lu, S., Li, D., Li, Y.** Intergranular Corrosion Behavior Associated with Delta-ferrite Transformation of Ti-modified Super304H Austenitic Stainless Steel *Corrosion Science* 90 2015: pp. 347 – 358.
https://doi.org/10.1016/j.corsci.2014.10.031

27. **Sun, Y., Moroz, A., Alrbaey, K.** Sliding Wear Characteristics and Corrosion Behaviour of Selective Laser Melted 316L Stainless Steel *Journal of Materials Engineering and Performance* 23 2014: pp. 518 – 526.
http://dx.doi.org/10.1007/s11665-013-0784-8

28. **Revie, R.W., Uhlig, H.H.** Corrosion and Corrosion Control. Wiley, New Jersey, 2008: pp. 120 – 123.
http://dx.doi.org/10.1002/9780470277270

29. **Roberge, P.R.** Corrosion Engineering: Principles and Practice. McGraw-Hill, New York, 2008: pp. 164 – 166.

30. **Oldfield, J.W., Sutton, W.H.** Crevice Corrosion of Stainless Steels: I. A Mathematical Model *British Corrosion Journal* 13 (1) 1978: pp. 13 – 22.
https://doi.org/10.1179/000705978798358671

31. **Geenen, K., Röttger, A., Theisen, W.** Corrosion Behavior of 316L Austenitic Steel Processed by Selective Laser Melting, Hot-isostatic Pressing, and Casting *Materials and Corrosion* 68 (7) 2017: pp. 764 – 775.
https://doi.org/10.1002/maco.201609210

32. **Schaller, R.F., Taylor, J.M., Rodelas, J., Schindelholz, E. J.** Corrosion Properties of Powder Bed Fusion Additively Manufactured 17-4 PH **S**tainless **S**teel *Corrosion* 73 (7) 2017: pp. 796 – 807.
https://doi.org/10.5006/2365